Research Article

Nano Research
2022, 15(3): 2558–2566

ISSN 1998-0124 CN 11-5974/O4
https://doi.org/10.1007/s12274-021-3751-y

Versatile $Ti_3C_2T_x$ MXene for free-radical scavenging

Jiang Liu[1,§], Wei Lu[1,§], Xifeng Lu[2], Lu Zhang[1], Haifeng Dong[3] (✉), and Yingchun Li[1] (✉)

[1] *Flexible Printed Electronics Technology Center and School of Science, Harbin Institute of Technology (Shenzhen), Shenzhen 518055, China*
[2] *Department of Physiology, Health Science Center, Shenzhen University, Shenzhen 518055, China*
[3] *Marshall Laboratory of Biomedical Engineering, Research Center for Biosensor and Nanotheranostic, School of Biomedical Engineering, Shenzhen University, Shenzhen 518055, China*
[§] *Jiang Liu and Wei Lu contributed equally to this work.*

Received: 26 May 2021 / **Revised:** 14 July 2021 / **Accepted:** 16 July 2021

ABSTRACT

MXene, as an emerging two-dimensional (2D) material with ultrathin structure and fascinating physiochemical properties, has been widely explored in broad applications. Versatile functions of MXenes are continuously explored. This work presents distinctive feature of MXene-$Ti_3C_2T_x$ nanosheets for free-radical (FRs) scavenging that never reported before. We demonstrated the mechanism and equation in regard to the reaction between $Ti_3C_2T_x$ and H_2O_2, which was applied to design colorimetric H_2O_2 strip assay with good performance. The good FRs scavenging capability of $Ti_3C_2T_x$, including a series of reactive oxygen species (ROS) and reactive nitrogen species (RNS), was systemically confirmed. The antioxidation capability of $Ti_3C_2T_x$ for protecting cells from oxidative damage was demonstrated using the oxidative damage model of alpha mouse liver 12 (AML-12) cells. This original work provides huge opportunities for MXenes in FR-related biomedical applications.

KEYWORDS

MXene, hydrogen peroxide, colorimetric sensor, reactive oxygen species, anti-oxidative damage

1 Introduction

Since the beginning of this century, two-dimensional (2D) nanomaterials, such as graphene [1], black phosphorous [2], and MoS_2 [3], have attracted great interest in many fields. Among 2D materials, a new family labeled as "MXenes" has received much attention for its innate and excellent features like high metallic conductivity, large surface area, and great hydrophilicity [4]. The general formula of MXene in composition is $M_{n+1}X_nT_x$, n = 1, 2, or 3, where M stands for transition metal, X represents C, and/or N, T means the surface group, and x denotes the corresponding amount [5]. Until now, more than 20 members in the MXene family have been synthesized [6], among which $Ti_3C_2T_x$ is one of the most widely studied ones [7].

Based on the unique features of $Ti_3C_2T_x$, scientists have carried out a series of attempts for exploring its biological applications. Due to its large surface area and abundant surface termination groups, $Ti_3C_2T_x$ has been applied in drug delivery [8], biosensing [9], blood purification [10], etc. $Ti_3C_2T_x$ possesses good optical absorption and photothermal conversion efficiency, enabling photoacoustic imaging and photothermal therapy [11, 12]. MXene quantum dots (QDs) have acted as a fluorescent probe for cell imaging or bio-target determination owing to the super small-size and luminous properties [13, 14].

Though some of its intriguing merits have been caved, the oxidation property of MXene has rarely been exploited and served practical needs [15–17]. Hydrogen peroxide and free radicals (FRs) are the main endogenous oxidants in organisms. H_2O_2 is the product of numerous enzymatic reactions, which is related to various physiological and pathological processes, and also acts as a crucial biomarker for disease diagnosis [18, 19]. FRs play a dual role as both deleterious and beneficial species [20–23]. Once oxidative stress and antioxidant defense are off balance, excessive FRs will cause damage to organism and even lead to severe diseases like metabolic disorder and cancer [24, 25]. Above all, it is meaningful to develop accurate H_2O_2 determination in different scenarios and find effective anti-oxidants for FRs scavenging [26–28]. The potential of $Ti_3C_2T_x$ in these two aspects is explored in this work, using H_2O_2 and FRs as the representative oxidants.

Herein, the reaction mechanism between $Ti_3C_2T_x$ and H_2O_2 was studied by characterizing the reaction process and analyzing the products. Based on this specific reaction, the following three applications of $Ti_3C_2T_x$ were established: Firstly, to satisfy quantitative and semi-quantitative requirements in different applications, two colorimetric methods for peroxide analysis were built based on spectroscopic absorption of reaction product and color variation of $Ti_3C_2T_x$-loaded paper strips. Next, the scavenging activities of $Ti_3C_2T_x$ towards various FRs including superoxide radical, hydroxyl radical, 1,1-diphenyl-2-picrylhydrazyl (DPPH) radical, and 2,2'-azino-bis(3-ethylbenzthiazoline-6-sulfonic acid (ABTS) radical were investigated by test-tube experiments. Afterwards, the biocompatibility of $Ti_3C_2T_x$ was evaluated using alpha mouse liver 12 (AML-12) cell line and its potential as an antioxidative reagent to improve cell viability under oxidative stress was studied using H_2O_2 induced oxidative damage model. Moreover, several technologies were applied to explore MXene uptake by cells.

Address correspondence to Haifeng Dong, hfdong@ustb.edu.cn; Yingchun Li, liyingchun@hit.edu.cn

2 Experimental

2.1 Preparation of MXene $Ti_3C_2T_x$

Multi-layer $Ti_3C_2T_x$ was prepared by etching MAX (Ti_3AlC_2) with LiF/HCl solution [29, 30]. Briefly, the etchant was obtained by mixing 2 g of LiF with 40 mL HCl (9 M) in a Teflon container under stirring (400 rpm) for 30 min. Then, 2 g of Ti_3AlC_2 powder was slowly added into the etchant. The mixture was stirred for 24 h at 35 °C and washed with deionized water using centrifugation and decantation until pH reached ~ 6. The precipitate was collected and dried in a vacuum oven at 60 °C overnight.

To prepare few-layer $Ti_3C_2T_x$, the multi-layer $Ti_3C_2T_x$ powder was dispersed in ethanol (as the intercalant), and sonicated for 30 min. After that, the sediment was collected by centrifugation for 10 min at 10,000 rpm and rinsed with deionized water. The sediment was re-dispersed in water and underwent centrifugation for 10 min at 3,500 rpm. Then the supernatant was collected, in which the $Ti_3C_2T_x$ was quantified by filtering the suspension with cellulose nitrate filter paper and measuring the weight of the filter paper after vacuum drying. Few-layer $Ti_3C_2T_x$ dispersions in phosphate buffer saline (PBS) and Dulbecco's minimum essential medium (DMEM) were prepared by centrifuging the above supernatant at 15,000 rpm for 10 min and washed with PBS or DMEM repeatedly to replace deionized water. Then the dispersions were sonicated for 3 h and the supernatants acquired by centrifugation at 6,000 rpm were preserved and applied for cell experiments.

2.2 Colorimetric detection for H_2O_2

5 mg·mL^{-1} multi-layer $Ti_3C_2T_x$ dispersions were mixed with H_2O_2 solutions at different concentrations at the volume ratio of 1:9 using a vortex mixer, and the suspensions were left still for 30 min at room temperature. Centrifugation at 5,000 rpm for 5 min was then carried out, and the supernatant was collected and adopted for ultraviolet–visible (UV–vis) detection. To measure the amount of H_2O_2 released from cells, HeLa cells were cultured in 6-well plates with a cell density of 3.0×10^5 cells/mL for 24 h. After the cultural medium was removed, 2.7 mL of phorbol myristate acetate (PMA) (200 ng·mL^{-1}) was added and incubated for 1 min with gentle shaking [31]. Then 0.3 mL of $Ti_3C_2T_x$ (5 mg·mL^{-1}) was added and incubated at room temperature for 30 min. After centrifugation, the UV–vis absorbance of the supernatant was measured.

2.3 Preparation of colorimetric strip

For preparing $Ti_3C_2T_x$-enabled test strip, different amounts of few-layer $Ti_3C_2T_x$ were dispersed in 100 mL of water and transferred evenly to a piece of qualitative filter paper by using a sand-core filtering funnel. Then the paper was dried in a vacuum oven and cut into 5 mm × 5 mm pieces. Finally, these paper pieces loaded with different amounts of few-layer $Ti_3C_2T_x$ were attached on a polyvinyl chloride sheet (5 mm × 75 mm) to form an array of strips applied for visual colorimetric detection of H_2O_2.

2.4 Free radical scavenging assay

Superoxide radical ($O_2^{\cdot -}$) scavenging: $O_2^{\cdot -}$ was produced by pyrogallol oxidation according to the report by Jia et al. [32]. After generation of $O_2^{\cdot -}$, 1 mL of multi-layer $Ti_3C_2T_x$ at different concentrations was added and incubated for 30 min. Then the mixture was centrifuged at 5,000 rpm for 5 min to subside excessive $Ti_3C_2T_x$, and the UV–vis absorption spectrum of the supernatant was measured. $O_2^{\cdot -}$ scavenging ability of MXene was assessed by the following formula Radical scavenging ratio (%) = $[(A_0 - A_1)/A_0] \times 100$, where A_0 and A_1 represent the absorbance of superoxide radical solution at 325 nm in the absence and presence of $Ti_3C_2T_x$. IC_{50} was identified as the dose of the antioxidant needed to eliminate half of the FRs.

Hydroxyl radical (•OH) scavenging: •OH was produced by the classical Fenton reaction [33]. 300 μL of H_2O_2 (1 mM) was added into 2 mL of mixture solution (consisting of 5 mM $FeSO_4$•$7H_2O$ and 5 mM salicylic acid-ethanol) to initiate the reaction. After 20 min, 1 mL of multi-layer $Ti_3C_2T_x$ was added and the mixture was incubated in dark for 30 min, followed by centrifugation. Absorbance of the supernatant at 510 nm was measured to calculate the scavenging ability based on the above formula.

DPPH radical scavenging: According to the report by Yin et al. [34], 0.1 mM DPPH ethanol solution was mixed with multi-layer $Ti_3C_2T_x$ dispersion at a ratio of 3:1 (v/v) and stored in dark for 30 min. The following procedure was the same as that in "Hydroxyl radical scavenging", except for the absorbance determined at 517 nm.

ABTS radical scavenging: A commercial total antioxidant capacity (T-AOC) assay kit was adopted and the ABTS radical working solution was prepared following the operating instruction. Then, 1 mL of the obtained solution was mixed with 50 μL of multi-layer $Ti_3C_2T_x$ and incubated in dark for 6 min. The next step was similar to the above assays except that the absorbance at 734 nm was taken.

2.5 Cytotoxicity test of H_2O_2

Cytotoxicity of H_2O_2 was evaluated by 3-(4,5-dimethyl-2-thiazolyl)-2,5-diphenyl-2H-tetrazolium bromide (MTT) assay and 20 mM acetaminophen (APAP) was adopted as the positive control. Briefly, AML-12 cells (1×10^4 cells/well) were seeded in 96-well plates and grew in DMEM/F-12 containing 10% fetal bovine serum (FBS) and 1% P/S under 5% CO_2 at 37 °C. After 24 h of incubation, the cells were treated with various concentrations of H_2O_2 (0–1.5 mM). After another 24 h incubation, the cells were washed with medium for several times, and then incubated with 0.5 mg·mL^{-1} MTT for 4 h. Subsequently, the medium was removed and replaced with 110 μL of dimethyl sulfoxide (DMSO). Cell viability was assessed based on the absorbance of purple formazan at 490 nm by the microplate reader. Meanwhile, the concentration of H_2O_2 needed to inhibit 50% of cell viability was defined as the median lethal dose (LD_{50}).

2.6 Cytotoxicity test of $Ti_3C_2T_x$

The cytotoxicity test of $Ti_3C_2T_x$ included MTT assay and CytoTox-Glo™ cytotoxicity assay. The former was similar to the above experiment, except that H_2O_2 was replaced by few-layer $Ti_3C_2T_x$ (0–300 μg·mL^{-1}). In the CytoTox-Glo™ cytotoxicity assay, 50 μL of assay reagents were added to the wells, which had been treated in the same way as that in MTT assay. After 15-min incubation at room temperature, the luminescence was measured by a Cytation 5 cell imaging multi-mode reader, which represents the luminescence of dead cells. Then, 50 μL of lysis reagents were added to lyse cells with incubation for 15 min. After that, the luminescence of total cells was measured. The cell viability was calculated according to the following formula Cell viability (%) $= \frac{I_i^{total} - I_i^{dead}}{I_c^{total} - I_c^{dead}} \times 100$, where I_i^{total} and I_c^{total} are the luminescene intensities of total cells with and without $Ti_3C_2T_x$ treatment, and I_i^{dead} and I_c^{dead} refer to the luminescence intensities of dead cells with and without $Ti_3C_2T_x$ treatment, respectively.

2.7 Antioxidation property of $Ti_3C_2T_x$ for H_2O_2-stimulated cells

Firstly, AML-12 cells were seeded and incubated in 96-well plates

for 24 h, followed by pretreatment with 50 μg·mL^{-1} few-layer $Ti_3C_2T_x$ for another 24 h. Then the cells were washed with medium and exposed to different concentrations of H_2O_2 (0.3, 0.5, and 0.7 mM) for another 24 h. A control group without $Ti_3C_2T_x$ and H_2O_2 treatment and a H_2O_2-treated group only with H_2O_2 treatment were set for comparison. The cell viability was calculated by measuring the absorbance value at 490 nm by the MTT assay. Annexin V-FITC apoptosis detection kit was adopted to evaluate the apoptosis of AML-12 cells. Briefly, the cells incubated in 12-well plates (1.5×10^5 cells/well) were firstly treated with 50 μg·mL^{-1} $Ti_3C_2T_x$ sheets and then with 0.5 or 0.7 mM H_2O_2. Afterward, total (attached and floating) cells were collected. The cell pellets were resuspended in 195 μL of binding buffer and stained with 5 μL of Annexin V-FITC as well as 10 μL of propidium iodide (PI) for 25 min in the dark. Later on, the cells were immediately analyzed by flow cytometry. APAP (20 mM) was adopted as the positive control and the number of cells analyzed for all samples were set as 10,000. $Ti_3C_2T_x$ uptake by cells was visually observed by three techniques, namely the inverted fluorescence microscopy, confocal microscopy, and transmission electron microscopy (TEM). The cell treatment processes are detailed in the Electronic Supplementary Material (ESM).

3 Results and discussion

3.1 Preparation and characterization of $Ti_3C_2T_x$

The main strategy of $Ti_3C_2T_x$ fabrication is wet-chemical etching of the precursor Ti_3AlC_2 (MAX) by hydrofluoric acid (HF) or HF-forming etchants, during which the weak metallic Ti–Al bonds are broken and the Al layer is selectively removed. Herein, wet-chemical etching was utilized for MXene synthesis [29, 30], in which LiF/HCl acted as the etchant for preparing multi-layer $Ti_3C_2T_x$ and ethanol was adopted as the intercalant to further weaken the interactions among layers for preparation of few-layer $Ti_3C_2T_x$. The synthesis process is outlined in Fig. 1(a). Morphology and structure of the materials were characterized by scanning electron microscopy (SEM), TEM, energy-dispersive spectroscopy (EDS), and elemental mapping. SEM images reveal the material changed notably from closely aligned layers (Fig. 1(b)) to loosely accordion-like multi-layered architecture (Fig. 1(c)) after etching of Al layers. In comparison with Ti_3AlC_2 (Fig. 1(d)), the percentage of aluminum markedly decreased in $Ti_3C_2T_x$ and meanwhile fluorine element appeared (Fig. 1(e)), implying the generation of numerous surface termination groups after etching.

Elemental mapping results (Figs. S1 and S2 in the ESM) confirm the above conclusion and suggest uniform dispersion of the termination groups. Furthermore, few-layer $Ti_3C_2T_x$ was synthesized by intercalating ethanol into multi-layer $Ti_3C_2T_x$. SEM and TEM images exhibit that the stacked structure of multi-layer $Ti_3C_2T_x$ was isolated into single or few flakes without overlapping (Fig. 1(f)). Notably, in this work, multi-layer $Ti_3C_2T_x$ was applied for colorimetric detection of H_2O_2 and elimination of FRs, while few-layer $Ti_3C_2T_x$ participated in fabrication of H_2O_2 test strip in that immobilization of few-layer $Ti_3C_2T_x$ on filter paper was firmer and more uniform than multi-layer $Ti_3C_2T_x$. In order to further reduce the particle size and promote the contact between $Ti_3C_2T_x$ and cells, the few-layer $Ti_3C_2T_x$ underwent ultrasonication for about 3 h before usage in cell experiments.

The particle sizes of the few-layer $Ti_3C_2T_x$ dispersed in H_2O, DMEM, and PBS were measured by a Zetasizer (Fig. 1(g)). The results indicate that $Ti_3C_2T_x$ displayed the optimal dispersibility in deionized water with an average particle size of 106 nm. When $Ti_3C_2T_x$ was dispersed in DMEM, agglomeration occurred and the particle size increased to 213 nm, while the dispersion in PBS yielded a larger particle size of about 2 μm. This phenomenon may be explained by the fact that the positive ions (Na^+, K^+) in PBS neutralize the initially negative charges of the surface-terminating groups of $Ti_3C_2T_x$ (–OH, –O, and –F), resulting in reduced electrostatic repulsion among $Ti_3C_2T_x$ nanosheets and leading to aggregation [35, 36].

3.2 Characterization of the reaction between $Ti_3C_2T_x$ and hydrogen peroxide

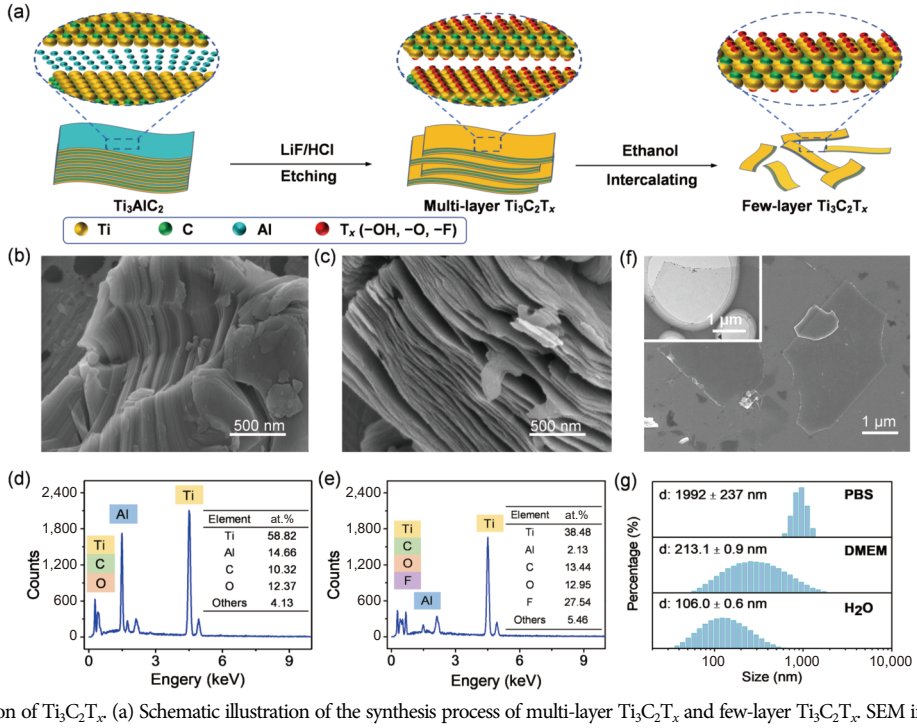

Figure 1 Characterization of $Ti_3C_2T_x$. (a) Schematic illustration of the synthesis process of multi-layer $Ti_3C_2T_x$ and few-layer $Ti_3C_2T_x$. SEM images of (b) Ti_3AlC_2 and (c) multi-layer $Ti_3C_2T_x$. EDS spectra and elemental percentage of (d) Ti_3AlC_2 and (e) multi-layer $Ti_3C_2T_x$. (f) SEM image of few-layer $Ti_3C_2T_x$. The inset of (f) is the TEM image of few-layer $Ti_3C_2T_x$. (g) Size distributions of few-layer $Ti_3C_2T_x$ dispersions in H_2O, DMEM, and PBS.

We accidentally discovered that exposure of $Ti_3C_2T_x$ dispersion to H_2O_2 solution caused color variation from black to bright yellow at room temperature, accompanying with gas generation and heat production (Fig. S3 in the ESM). Specificity of the reaction was investigated by incubating multi-layer $Ti_3C_2T_x$ with various inorganic acids and strong oxidants, including aqua regia, nitric acid, hydrochloric acid, sulfuric acid, hydrofluoric acid, acetic acid, and sodium hypochlorite. Except for aqua regia and nitric acid, no obvious changes were observed between $Ti_3C_2T_x$ and the other reagents (Fig. S4 in the ESM). Notably, the reaction rate of $Ti_3C_2T_x$ with H_2O_2 was significantly faster than that with nitric acid, and similar to that with aqua regia (the well-known strong corrosive substance). Specificity of the reaction between $Ti_3C_2T_x$ and H_2O_2 may be ascribed to the strong oxidizing property of H_2O_2 and the high affinity between titanium and oxygen atoms [37]. Notably, when MXene was replaced with MAX, it failed to observe color alteration after exposure to H_2O_2 for 24 h (Fig. S5 in the ESM), which may be attributed to the existence of Al layer that inhibited the contact of H_2O_2 with internal Ti and C layers. In comparison, the high reactivity of H_2O_2 towards $Ti_3C_2T_x$ MXene can be explained by the fact that the reactive oxygen attacks the exposed Ti atom layer, which has been demonstrated by density functional theory (DFT) calculation [27, 28].

In order to further investigate the reaction mechanism between H_2O_2 and $Ti_3C_2T_x$, the produced residues and gases after sufficient reaction were collected and identified. Firstly, SEM, X-ray photoelectron spectroscopy (XPS), and EDS were used to characterize the residues of yellow powder (Fig. S6(a) in the ESM). SEM images display amorphous particles (Figs. S6(b) and S6(c) in the ESM) and the fully scanned XPS spectrum demonstrates the existence of O, Ti, C, and F elements (Fig. S6(d) in the ESM). The peaks of Ti $2p_{3/2}$ and Ti $2p_{1/2}$ are located at 459.0 and 464.7 eV, indicating that titanium is present in a single oxidation state of Ti^{4+} (Fig. 2(a)) [38, 39]. The C 1s spectrum shows three peaks at 284.8, 286.6, and 289.1 eV, corresponding to the C–C, C–O, and O–C=O bond, respectively (Fig. 2(b)) [15]. And the O 1s spectrum exhibits the presence of the Ti–O (530.4 eV), C–O (531.2 eV), –OH (531.9 eV), and C=O (532.6 eV) bond (Fig. 2(c)) [38, 40]. It can be inferred that the residues are mainly composed of graphite oxide and titanium peroxide. The latter may be the reaction product of Ti^{4+} and H_2O_2 [38]. It is noticed that the content of oxygen in the residues greatly increased and the amount of carbon decreased (Fig. 2(d)) compared with that in $Ti_3C_2T_x$ (Fig. 1(e)). Secondly, the produced gases were identified to be oxygen (99.41% ± 0.06%, *w*/*w*), carbon monoxide (0.24% ± 0.01%, *w*/*w*), and carbon dioxide (0.35% ± 0.05%, *w*/*w*) (Fig. S7 in the ESM) by gas chromatography (the experimental details are described in the ESM). Therefore, the reaction between $Ti_3C_2T_x$ and H_2O_2 is very likely to be described as $Ti_3C_2T_x + H_2O_2 \rightarrow$ titanium peroxide + graphite oxide + $H_2O + O_2\uparrow + CO\uparrow + CO_2\uparrow$.

In addition, the morphology of multi-layer $Ti_3C_2T_x$ exposed to low concentrations of H_2O_2 was characterized by SEM to acquire detailed information from the micro perspective. When $Ti_3C_2T_x$ was exposed to 1 μM H_2O_2, some pores deep into the interior of $Ti_3C_2T_x$ were observed, and the diameters of the pores ranging from 80 to 130 nm (Fig. 2(e)). The increase of H_2O_2 concentration brought about increased amount and enlarged diameter of pores (Fig. S8(a) in the ESM). When H_2O_2 concentration exceeded 20 μM, lots of pores were generated, inducing collapse of the multi-layered structure of $Ti_3C_2T_x$ (Fig. S8(b) in the ESM). Unlike regular layer-by-layer etching from the outside to the inside, the corrosion between multi-layer $Ti_3C_2T_x$ and H_2O_2 might be described as below. H_2O_2 first attacks the active sites on the surface of $Ti_3C_2T_x$ and then penetrates into its interior to form pores throughout the multi-layed structure longitudinally. Subsequently, the pore size grows gradually until the structure collapses (Fig. 2(f)). This discovery may be utilized for controllable and efficient preparation of nano/meso-porous MXene, the pore diameter of which can be easily adjusted by changing H_2O_2 concentration. The porous MXene obtained by this strategy may have some promising applications in the fields of catalysis, membrane separation, energy storage, drug delivery system, etc.

3.3 Colorimetric detection for H_2O_2

In order to verify the feasibility of the colorimetric method in detecting H_2O_2, $Ti_3C_2T_x$ was added into different concentrations

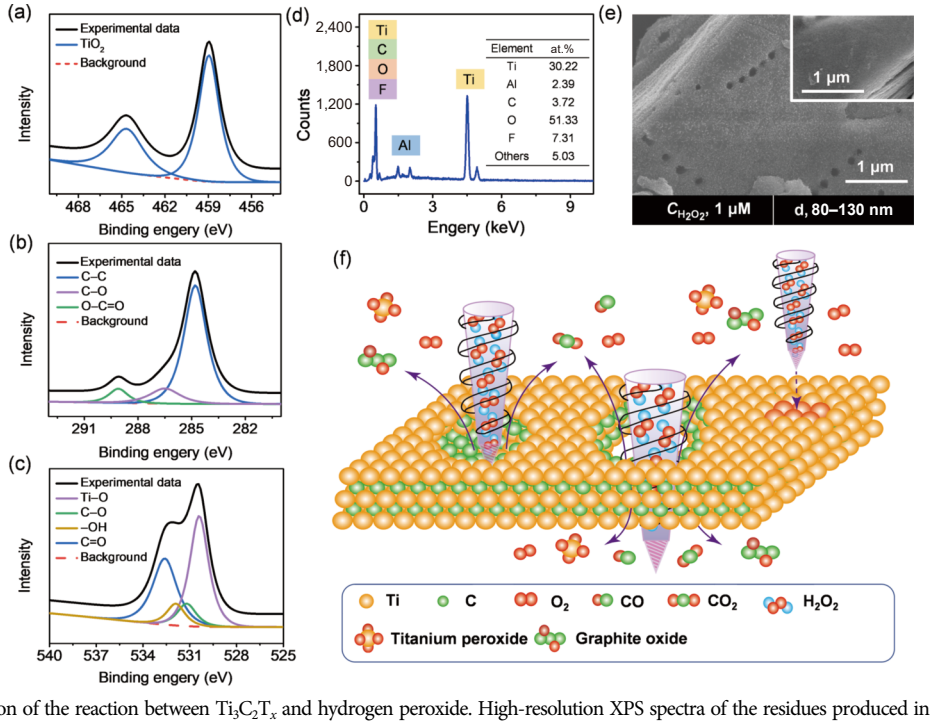

Figure 2 Characterization of the reaction between $Ti_3C_2T_x$ and hydrogen peroxide. High-resolution XPS spectra of the residues produced in the reaction ((a) Ti 2p, (b) C 1s, and (c) O 1s). (d) EDS spectrum and elemental percentage of the residues. (e) SEM image of $Ti_3C_2T_x$ (5 mg·mL^{-1}) before (the inset) and after being exposed to 1 μM H_2O_2 for 24 h. (f) Illustration of the reaction mechanism of $Ti_3C_2T_x$ and H_2O_2.

of H_2O_2, and the resulting products were analyzed by the UV–vis spectrometer. After sedimentation of excess MXene via centrifugation, the color of the supernatants changed from colorless to bright yellow with the increase of H_2O_2 concentration (Fig. S9 in the ESM), which is ascribed to the generation of yellow titanium peroxide. The maximum UV–vis absorbance (A) of the supernatants was at 370 nm (Fig. 3(a)), and linearly correlated with H_2O_2 concentration (C) from 5.0 μM to 0.5 mM and 0.5 mM to 5.0 mM (Fig. 3(b)). The corresponding regression equations are $A = 0.3334C + 0.0140$ ($R^2 = 0.9915$) and $A = 0.2983C + 0.0331$ ($R^2 = 0.9989$), respectively, with the limit of detection (LOD) of 1.0 μM ($S/N = 3$). Compared with other colorimetric strategies for H_2O_2 detection, the presented method yields lower LOD and wider linear range (Table S1 in the ESM). And the LOD presented in this work meets the requirement of early clinical diagnosis, in which the concentration threshold of H_2O_2 for cell damage is 50 μM [41]. Significantly, no other reagent is required and the detection process is more convenient than the previous colorimetric determination for H_2O_2, in which chromogenic agent such as 3,3',5,5'-tetramethylbenzidine (TMB), o-phenylenediamine (OPD), and ABTS is indispensable (Table S1 in the ESM). Therefore, this new colorimetric assay not only develops a sensitive way for H_2O_2 detection, but also offers a different strategy to carry forward the utilization of MXene in biosensing.

To further evaluate the performance of this established method, H_2O_2 released from HeLa cells was quantified. PMA was adopted as the stimulating agent to induce H_2O_2 generation [31]. $Ti_3C_2T_x$ was added to the 6-well plates and the UV–vis absorbance was measured by a spectrometer (Fig. S10 in the ESM). The concentration of H_2O_2 was calculated to be 8.04 μM and the corresponding mass of H_2O_2 released from a single cell was about 2.68 fmol, which is in the similar order of magnitude to some other reported methods (Table S2 in the ESM) [42, 43].

In consideration of practicability in some scenarios, a $Ti_3C_2T_x$-enabled test strip was further built for H_2O_2 semi-quantification. The strip consisted of six paper sheets loaded with different amounts of $Ti_3C_2T_x$ and one sheet without $Ti_3C_2T_x$ as the reference. The amount of $Ti_3C_2T_x$ loaded in the six sheets corresponded to a specific H_2O_2 concentration ranging from 0.05 to 100 mM (Fig. 3(c)). When the strip was immersed in H_2O_2 solution, $Ti_3C_2T_x$ on the sheets would be involved in reacting with H_2O_2 and be consumed gradually, accompanied by color change of the sheets from black or grey to white. Hence, semi-quantification of H_2O_2 can be realized via observing color fading of the sheets after 2-h incubation (Fig. 3(c)). Since the newly fabricated test strip is free from natural enzymes, it may adapt to harsh conditions such as strong acid/alkali and extreme temperature.

3.4 The radical-scavenging capability of $Ti_3C_2T_x$

The property of $Ti_3C_2T_x$ in eliminating H_2O_2 illuminates its potential in scavenging FRs, and herein a series of reactive oxygen species (ROS) and reactive nitrogen species (RNS) were employed to systematically evaluate the performance of $Ti_3C_2T_x$ in disposing of FRs. Firstly, two physiologically relevant ROS, superoxide anion radical ($O_2^{\bullet -}$) and hydroxyl radical (•OH), were selected to evaluate the ROS-scavenging capacity of $Ti_3C_2T_x$. $O_2^{\bullet -}$ was prepared by autooxidation decomposition of pyrogallol [44]. Prior to addition of $Ti_3C_2T_x$, the $O_2^{\bullet -}$ solution presented pale yellow and had the maximum absorption at 325 nm. After incubation with $Ti_3C_2T_x$, the solution changed to colorless and the absorbance was markedly decreased (Figs. 3(d) and 3(e)). With the increase of $Ti_3C_2T_x$ concentration from 5.0 μg·mL^{-1} to 7.5 mg·mL^{-1}, the $O_2^{\bullet -}$ scavenging rate increased and then reached the equilibrium state (Fig. 3(e)). IC_{50}, identified as the dose of antioxidant needed to eliminate half of FRs, was calculated to be 1.4 mg·mL^{-1} for $O_2^{\bullet -}$.

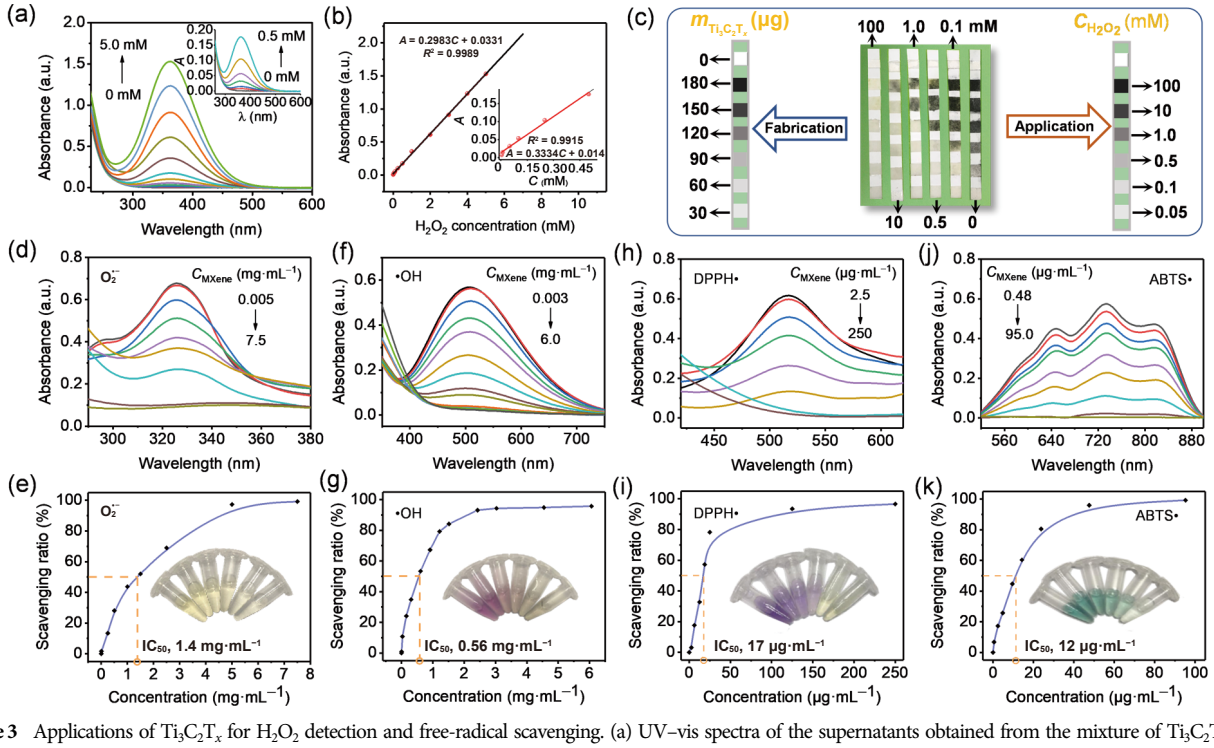

Figure 3 Applications of $Ti_3C_2T_x$ for H_2O_2 detection and free-radical scavenging. (a) UV–vis spectra of the supernatants obtained from the mixture of $Ti_3C_2T_x$ and H_2O_2 (0–5.0 mM). Inset is the amplified UV–vis spectra ($C_{H_2O_2}$, 0–0.5 mM). (b) Calibration curves of UV–vis absorbance vs. $C_{H_2O_2}$ (0.5–5.0 mM). Inset is the amplified calibration curve ($C_{H_2O_2}$, 0.005–0.5 mM). (c) Illustration of the $Ti_3C_2T_x$-enabled test strip containing several paper sheets loaded with different amounts of $Ti_3C_2T_x$, photographs of the test strips after immersion in H_2O_2 (0.1–100 mM), and the concentration of H_2O_2 corresponding to each sheet. The UV–vis spectra of different FRs ((d) $O_2^{\bullet -}$, (f) •OH, (h) DPPH•, and (j) ABTS•) incubated with $Ti_3C_2T_x$ at different concentration ranges ((d) 0.005–7.5 mg·mL^{-1}, (f) 0.003–6.0 mg·mL^{-1}, (h) 2.5–250 μg·mL^{-1}, and (j) 0.48–95 μg·mL^{-1}). Capacity of $Ti_3C_2T_x$ in scavenging (e) $O_2^{\bullet -}$, (g) •OH, (i) DPPH•, and (k) ABTS•. Insets are the photographs of the FRs reacting with different concentrations of $Ti_3C_2T_x$.

Next, •OH was produced by the classical Fenton reaction between H_2O_2 and Fe^{2+} [33]. Absorption of the •OH solution at 510 nm decreased significantly after incubation with $Ti_3C_2T_x$ (Fig. 3(f)) and color of the solution changed from purple to colorless with the increase of $Ti_3C_2T_x$ concentrations (Fig. 3(g)). The IC_{50} value was calculated to be 0.56 mg·mL^{-1}.

DPPH and ABTS radicals are the model FRs frequently used in laboratory assays for evaluating the radical scavenging ability of target substances [45]. The performance in DPPH• and ABTS· elimination represents anti-RNS and total antioxidative ability, respectively. As shown in Figs. 3(h) and 3(i), DPPH• solution displayed dark purple with a maximum absorption at 517 nm. After incubation with $Ti_3C_2T_x$, the DPPH• solution turned to pale yellow (Fig. 3(i)) and the peak intensity declined as the concentration of $Ti_3C_2T_x$ increased from 2.5 to 250 μg·mL^{-1} (Fig. 3(h)). Similar to DPPH• scavenging, the peak intensity at 734 nm belonging to ABTS• gradually fell down as the $Ti_3C_2T_x$ concentration increased (Fig. 3(j)) and the color converted from green to colorless (Fig. 3(k)). The IC_{50} values for DPPH· and ABTS• were 17 and 12 μg·mL^{-1}, respectively, which are superior to most of the reported FRs scavengers including nanomaterials and natural substances (Table S3 in the ESM). In addition, MXene may gain wider application than the existing antioxidants for its excellent thermal and light stability [46].

We speculate the mechanism for FRs scavenging is that FRs lack electrons and have unpaired electrons, while MXene is an electron-rich nanomaterial [47, 48], which can provide electrons to pair with the unpaired electrons in FRs. Meanwhile, the remarkable FRs scavenging capability of $Ti_3C_2T_x$ may be attributed to the following characteristics: (1) $Ti_3C_2T_x$ is composed of alternating Ti and C layers combined via weak van der Waals forces, affording high chemical reaction activity; (2) the layer-packed structure of $Ti_3C_2T_x$ facilitates fast electron transfer among radicals and $Ti_3C_2T_x$; (3) the abundant functional groups on the surface contribute to the scavenging capacity of MXene [49, 50].

3.5 Antioxidative property of $Ti_3C_2T_x$ against cell injury

Based on its great radical-scavenging ability, $Ti_3C_2T_x$ may serve as an agent against oxidative damage *in vitro*. Firstly, the biotoxicity of $Ti_3C_2T_x$ was investigated by two typical methods and both suggested low cytotoxicity of $Ti_3C_2T_x$. Particularly, MTT assay showed that the cell viability was close to 100% after 24 h incubation with $Ti_3C_2T_x$ in the concentration range of 25–100 μg·mL^{-1} (Fig. 4(a)). CytoTox-Glo™ cytotoxicity assay revealed that $Ti_3C_2T_x$ at a concentration as high as 200 μg·mL^{-1} did not induce significant changes of cell viability (Fig. 4(b)). In addition, the main oxidation products of $Ti_3C_2T_x$, identified as titanium peroxide, graphite oxide, and O_2 in this work (Figs. 2(a)–2(c)), have long been regarded to be biocompatible [51, 52]. Moreover, the low percentage (0.24%) of the produced CO may even have cytoprotective effects [53]. Therefore, encouraged by the excellent radical scavenging ability of $Ti_3C_2T_x$ and the low toxicity of both $Ti_3C_2T_x$ and its products, we evaluated the cell-protecting ability of $Ti_3C_2T_x$ toward H_2O_2-stimulated AML-12 cells. Figure 4(c) shows that the viability of cells decreased gradually with increasing the concentrations of H_2O_2. When the concentration of H_2O_2 was higher than 0.25 mM, there was a significant difference after H_2O_2 treatment and the median LD_{50} was calculated as 0.55 mM, implying occurrence of serious oxidative damage in cells.

After that, the antioxidative effect of $Ti_3C_2T_x$ under H_2O_2 stimulation was further evaluated by MTT and flow cytometry assay. AML-12 cells underwent different treatments, as described in the Materials and methods and illustrated in Table S4 in the ESM. As shown in Fig. 4(d), under H_2O_2 stimulations, cells pretreated with $Ti_3C_2T_x$ exhibited higher viability, in comparison with those without pretreatment. Furthermore, by comparing the percentage of living and apoptotic cells in $Ti_3C_2T_x$-pretreated group and H_2O_2-treated group, one can conclude that H_2O_2-induced apoptosis was remarkably alleviated by introduction of $Ti_3C_2T_x$ in cells (Figs. 4(e) and 4(f)). The above results reveal that $Ti_3C_2T_x$ possesses antioxidative capability against oxidative stress.

In order to explore the protection mechanism of $Ti_3C_2T_x$ towards cells, the endocytosis of $Ti_3C_2T_x$ was investigated by fluorescence microscopy, confocal microscopy, and TEM. Firstly, a fluorescent nanocomposite of $Ti_3C_2T_x$ and doxorubicin (Dox), $Ti_3C_2T_x$@Dox, was prepared and incubated with AML-12 cells for 24 h. As shown in Fig. S11 in the ESM, the bright red fluorescence belonging to $Ti_3C_2T_x$@Dox was observed in cells, suggesting the successful internalization of $Ti_3C_2T_x$. Confocal microscopy (Fig. S12 in the ESM) and TEM (Fig. 4(g) , Fig. S13 in the ESM) show the similar results, wherein $Ti_3C_2T_x$ was found inside cells. Since its particle size is about 200 nm (Fig. 1(g)), clathrin-mediated endocytosis may be the main pathway during internalization of $Ti_3C_2T_x$ [54]. On the basis of the above results, the protective function of MXene against oxidative stress is more likely to take place intracellularly, as vividly illustrated in Fig. 4(h).

4 Conclusions

In this work, we have carried out a series of studies to explore the oxidation property of $Ti_3C_2T_x$ and to cave its applications based on this feature. Through the study of the reaction mechanism between $Ti_3C_2T_x$ and hydrogen peroxide, the reaction products were verified to be titanium peroxide, graphite oxide, O_2, CO, and CO_2. Besides, it was observed that the corrosion of H_2O_2 toward $Ti_3C_2T_x$ is similar to a "drilling" process accompanied by the formation of nano/meso pores, which may be employed as a facile and efficient strategy to prepare porous MXene. Moreover, based on the color alteration occurring during the reaction, two colorimetric methods of H_2O_2 detection were established via either UV–vis spectrophotometer or test paper strip, providing precise determination or quasi-quantification in accordance with different analytical requirements. The outstanding FRs-scavenging abilities of $Ti_3C_2T_x$ towards $O_2^{\cdot -}$, •OH, DPPH•, and ABTS• were fully confirmed by test-tube experiments, in which the scavenging capacity for DPPH• and ABTS• was superior to most of the reported scavengers from the natural compounds and artificial materials. Finally, the antioxidative effect of $Ti_3C_2T_x$ for cells against H_2O_2-induced injury was proved by both MTT and flow cytometry assay, and the protection may occur inside cells through endocytosis of $Ti_3C_2T_x$. All in all, the versatile $Ti_3C_2T_x$ was successfully applied in H_2O_2 determination, FRs scavenging, and protection for live cells against oxidation damage.

On the basis of the above findings, we could foresee several applications of MXene in these aspects: (1) MXene-involved colorimetric sensing platform can be further developed as a universal detection strategy for other oxides including various FRs; (2) MXene may play a part in preparing sunblock and other sunscreen products owing to its decent capability of absorbing UV light and further getting rid of FRs arising from sunlight; (3) MXene could serve as a highly effective antioxidant in regulating the oxidative stress in organism; (4) a drug delivery system based on MXene may exert antioxidative activity to the utmost, in which MXene could act as a scavenger to eliminate FRs and meanwhile as a carrier for loading other active substances. This work may open a new horizon for MXene-derived materials applied in extensive fields especially in biomedicine. However, the antioxidation mechanism of MXene and the specific reactions between MXene and peroxides are still far from clear and further exploration is needed in the aspects of theoretical simulation and

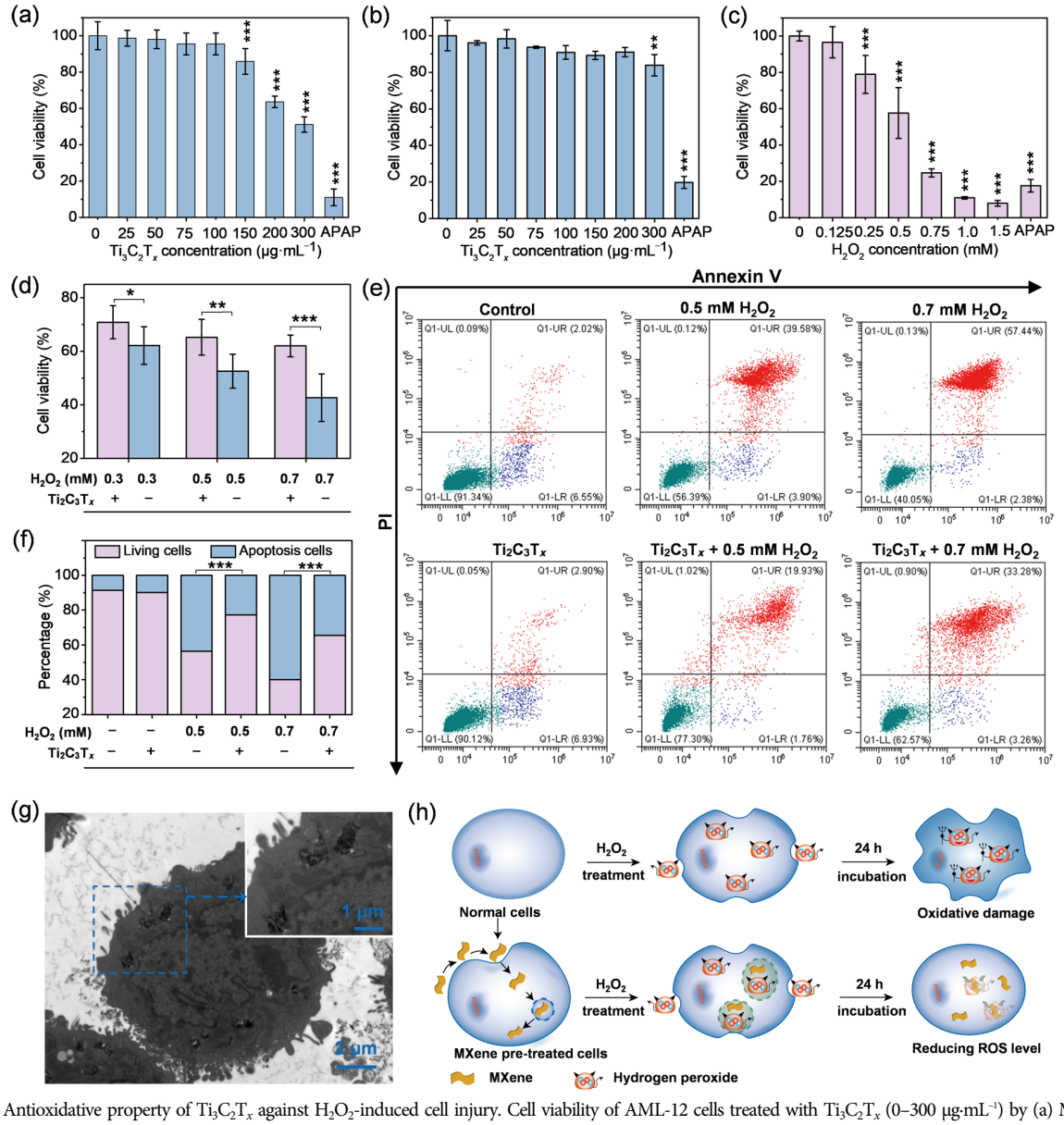

Figure 4 Antioxidative property of $Ti_3C_2T_x$ against H_2O_2-induced cell injury. Cell viability of AML-12 cells treated with $Ti_3C_2T_x$ (0–300 μg·mL^{-1}) by (a) MTT assay and (b) CytoTox-GloTM cytotoxicity assay. (c) Cell viability of AML-12 cells treated with H_2O_2 (0–1.5 mM) by MTT assay. (d) Cell viability of AML-12 cells in H_2O_2 environment (0.3, 0.5, and 0.7 mM) with and without $Ti_3C_2T_x$ (50 μg·mL^{-1}) pretreatment. (e) Flow cytometry assay for AML-12 cells under different treatments determined by Annexin V/PI staining and (f) the corresponding statistical chart for apoptotic cells and living cells. (g) TEM images of AML-12 cells treated with 50 μg·mL^{-1} $Ti_3C_2T_x$. (h) Schematic illustration of the intracellular protective effect of MXene. All data are presented as the mean ± standard deviation (SD). Asterisk indicates a significant difference: $^*P < 0.05$, $^{**}P < 0.01$, $^{***}P < 0.001$.

practical experiments.

Acknowledgements

This work was financially supported by the Key Program of Natural Science Foundation of Shenzhen (No. JCYJ20200109113410174), the National Natural Science Foundation of China (No. 81973280), the Key Technique Improvement of Xinjiang Licorice Planting and Quality Control of Xinjiang Production & Construction Corps (No. 2018AB012), and Guangdong Province Covid-19 Pandemic Control Research Fund (No. 2020KZDZX1223). We thank Wengui Nie from Shihezi University for her work in supplementing the gas characterization experiments.

Electronic Supplementary Material: Supplementary material (further details of the experimental procedures, investigation of the reaction between $Ti_3C_2T_x$ and other oxidants, the characterization of endocytosis of cells for $Ti_3C_2T_x$, and the comparison of different antioxidants for scavenging free radicals) is available in the online version of this article at https://doi.org/10.1007/s12274-021-3751-y.

References

[1] Wu, J.; Feng, S. L.; Wei, X. Z.; Shen, J.; Lu, W. Q.; Shi, H. F.; Tao, K.; Lu, S. R.; Sun, T.; Yu, L. Y. et al. Facile synthesis of 3D graphene flowers for ultrasensitive and highly reversible gas sensing. *Adv. Funct. Mater.* **2016**, *26*, 7462–7469.

[2] Cho, S. Y.; Lee, Y.; Koh, H. J.; Jung, H.; Kim, J. S.; Yoo, H. W.; Kim, J.; Jung, H. T. Superior chemical sensing performance of black phosphorus: Comparison with MoS_2 and graphene. *Adv. Mater.* **2016**, *28*, 7020–7028.

[3] Cho, S. Y.; Kim, S. J.; Lee, Y.; Kim, J. S.; Jung, W. B.; Yoo, H. W.; Kim, J.; Jung, H. T. Highly enhanced gas adsorption properties in vertically aligned MoS_2 layers. *ACS Nano* **2015**, *9*, 9314–9321.

[4] Zhang, J. F.; Cao, H. Y.; Wang, H. B. Research progress of novel

two-dimensional material MXene. *J. Inorg. Mater.* **2017**, *32*, 561–570.

[5] Naguib, M.; Kurtoglu, M.; Presser, V.; Lu, J.; Niu, J. J.; Heon, M.; Hultman, L.; Gogotsi, Y.; Barsoum, M. W. Two-dimensional nanocrystals produced by exfoliation of Ti_3AlC_2. *Adv. Mater.* **2011**, *23*, 4248–4253.

[6] Hu, Q. K.; Sun, D. D.; Wu, Q. H.; Wang, H. Y.; Wang, L. B.; Liu, B. Z.; Zhou, A. G.; He, J. L. Mxene: A new family of promising hydrogen storage medium. *J. Phys. Chem. A* **2013**, *117*, 14253–14260.

[7] Alhabeb, M.; Maleski, K.; Anasori, B.; Lelyukh, P.; Clark, L.; Sin, S.; Gogotsi, Y. Guidelines for synthesis and processing of two-dimensional titanium carbide ($Ti_3C_2T_x$ MXene). *Chem. Mater.* **2017**, *29*, 7633–7644.

[8] Han, X. X.; Huang, J.; Lin, H.; Wang, Z. G.; Li, P.; Chen, Y. 2D ultrathin MXene-based drug-delivery nanoplatform for synergistic photothermal ablation and chemotherapy of cancer. *Adv. Healthc. Mater.* **2018**, *7*, 1701394.

[9] Liu, J.; Jiang, X. T.; Zhang, R. Y.; Zhang, Y.; Wu, L. M.; Lu, W.; Li, J. Q.; Li, Y. C.; Zhang, H. MXene-enabled electrochemical microfluidic biosensor: Applications toward multicomponent continuous monitoring in whole blood. *Adv. Funct. Mater.* **2019**, *29*, 1807326.

[10] Meng, F. Y.; Seredych, M.; Chen, C.; Gura, V.; Mikhalovsky, S.; Sandeman, S.; Ingavle, G.; Ozulumba, T.; Miao, L.; Anasori, B. et al. MXene sorbents for removal of urea from dialysate: A step toward the wearable artificial kidney. *ACS Nano* **2018**, *12*, 10518–10528.

[11] Zong, L. Y.; Wu, H. X.; Lin, H.; Chen, Y. A polyoxometalate-functionalized two-dimensional titanium carbide composite MXene for effective cancer theranostics. *Nano Res.* **2018**, *11*, 4149–4168.

[12] Cao, Y.; Wu, T. T.; Zhang, K.; Meng, X. D.; Dai, W. H.; Wang, D. D.; Dong, H. F.; Zhang, X. J. Engineered exosome-mediated near-infrared-ii region V_2C quantum dot delivery for nucleus-target low-temperature photothermal therapy. *ACS Nano* **2019**, *13*, 1499–1510.

[13] Xue, Q.; Zhang, H. J.; Zhu, M. S.; Pei, Z. X.; Li, H. F.; Wang, Z. F.; Huang, Y.; Huang, Y.; Deng, Q. H.; Zhou, J. et al. Photoluminescent Ti_3C_2 MXene quantum dots for multicolor cellular imaging. *Adv. Mater.* **2017**, *29*, 1604847.

[14] Guo, Z.; Zhu, X. H.; Wang, S. G.; Lei, C. Y.; Huang, Y.; Nie, Z.; Yao, S. Z. Fluorescent Ti_3C_2 MXene quantum dots for an alkaline phosphatase assay and embryonic stem cell identification based on the inner filter effect. *Nanoscale* **2018**, *10*, 19579–19585.

[15] Ahmed, B.; Anjum, D. H.; Hedhili, M. N.; Gogotsi, Y.; Alshareef, H. N. H_2O_2 assisted room temperature oxidation of Ti_2C MXene for li-ion battery anodes. *Nanoscale* **2016**, *8*, 7580–7587.

[16] Ghassemi, H.; Harlow, W.; Mashtalir, O.; Beidaghi, M.; Lukatskaya, M. R.; Gogotsi, Y.; Taheri, M. L. *In situ* environmental transmission electron microscopy study of oxidation of two-dimensional Ti_3C_2 and formation of carbon-supported TiO_2. *J. Mater. Chem. A* **2014**, *2*, 14339–14343.

[17] Naguib, M.; Mashtalir, O.; Lukatskaya, M. R.; Dyatkin, B.; Zhang, C. F.; Presser, V.; Gogotsi, Y.; Barsoum, M. W. One-step synthesis of nanocrystalline transition metal oxides on thin sheets of disordered graphitic carbon by oxidation of MXenes. *Chem. Commun.* **2014**, *50*, 7420–7423.

[18] Diehn, M.; Cho, R. W.; Lobo, N. A.; Kalisky, T.; Dorie, M. J.; Kulp, A. N.; Qian, D. L.; Lam, J. S.; Ailles, L. E.; Wong, M. et al. Association of reactive oxygen species levels and radioresistance in cancer stem cells. *Nature* **2009**, *458*, 780–783.

[19] Song, Z. G.; Kwok, R. T. K.; Ding, D.; Nie, H.; Lam, J. W. Y.; Liu, B.; Tang, B. Z. An AIE-active fluorescence turn-on bioprobe mediated by hydrogen-bonding interaction for highly sensitive detection of hydrogen peroxide and glucose. *Chem. Commun.* **2016**, *52*, 10076–10079.

[20] Dickinson, B. C.; Chang, C. J. Chemistry and biology of reactive oxygen species in signaling or stress responses. *Nat. Chem. Biol.* **2011**, *7*, 504–511.

[21] He, S. S.; Jiang, Y. Y.; Li, J. C.; Pu, K. Y. Semiconducting polycomplex nanoparticles for photothermal ferrotherapy of cancer. *Angew. Chem., Int. Edit.* **2020**, *59*, 10633–10638.

[22] Zhu, H. J.; Fang, Y.; Miao, Q. Q.; Qi, X. Y.; Ding, D.; Chen, P.; Pu, K. Y. Regulating near-infrared photodynamic properties of semiconducting polymer nanotheranostics for optimized cancer therapy. *ACS Nano* **2017**, *11*, 8998–9009.

[23] Jiang, Y. Y.; Zhao, X. H.; Huang, J. G.; Li, J. C.; Upputuri, P. K.; Sun, H.; Han, X.; Pramanik, M.; Miao, Y. S.; Duan, H. W. et al. Transformable hybrid semiconducting polymer nanozyme for second near-infrared photothermal ferrotherapy. *Nat. Commun.* **2020**, *11*, 1857.

[24] Liu, Y. L.; Ai, K. L.; Ji, X. Y.; Askhatova, D.; Du, R.; Lu, L. H.; Shi, J. J. Comprehensive insights into the multi-antioxidative mechanisms of melanin nanoparticles and their application to protect brain from injury in ischemic stroke. *J. Am. Chem. Soc.* **2017**, *139*, 856–862.

[25] Losada-Barreiro, S.; Bravo-Díaz, C. Free radicals and polyphenols: The redox chemistry of neurodegenerative diseases. *Eur. J. Med. Chem.* **2017**, *133*, 379–402.

[26] Jastrzebska, A.; Szuplewska, A.; Rozmysłowska-Wojciechowska, A.; Mitrzak, J.; Wojciechowski, T.; Chudy, M.; Moszczyńska, D.; Wójcik, A.; Prenger, K.; Naguib, M. Juggling surface charges of 2D niobium carbide MXenes for a reactive oxygen species scavenging and effective targeting of the malignant melanoma cell cycle into programmed cell death. *ACS Sustainable Chem. Eng.* **2020**, *8*, 7942–7951.

[27] Feng, W.; Han, X. G.; Hu, H.; Chang, M. Q.; Ding, L.; Xiang, H. J.; Chen, Y.; Li, Y. H. 2D vanadium carbide MXenzyme to alleviate ROS-mediated inflammatory and neurodegenerative diseases. *Nat. Commun.* **2021**, *12*, 2203.

[28] Ren, X. Y.; Huo, M. F.; Wang, M. M.; Lin, H.; Zhang, X. X.; Yin, J.; Chen, Y.; Chen, H. H. Highly catalytic niobium carbide (MXene) promotes hematopoietic recovery after radiation by free radical scavenging. *ACS Nano* **2019**, *13*, 6438–6454.

[29] Liu, J.; Zhang, H. B.; Sun, R. H.; Liu, Y. F.; Liu, Z. S.; Zhou, A. G.; Yu, Z. Z. Hydrophobic, flexible, and lightweight MXene foams for high-performance electromagnetic-interference shielding. *Adv. Mater.* **2017**, *29*, 1702367.

[30] Zhao, X.; Zha, X. J.; Pu, J. H.; Bai, L.; Bao, R. Y.; Liu, Z. Y.; Yang, M. B.; Yang, W. Macroporous three-dimensional MXene architectures for highly efficient solar steam generation. *J. Mater. Chem. A* **2019**, *7*, 10446–10455.

[31] Shi, Q. R.; Song, Y.; Zhu, C. Z.; Yang, H. P.; Du, D.; Lin, Y. H. Mesoporous Pt nanotubes as a novel sensing platform for sensitive detection of intracellular hydrogen peroxide. *ACS Appl. Mater. Interfaces* **2015**, *7*, 24288–24295.

[32] Jia, J.; Lin, B.; Gao, Y. F.; Jiao, Y.; Li, L.; Dong, C.; Shuang, S. M. Highly luminescent N-doped carbon dots from black soya beans for free radical scavenging, Fe^{3+} sensing and cellular imaging. *Spectrochim. Acta Part A: Mol. Biomol. Spectrosc.* **2019**, *211*, 363–372.

[33] Zhao, S. J.; Lan, M. H.; Zhu, X. Y.; Xue, H. T.; Ng, T. W.; Meng, X. M.; Lee, C. S.; Wang, P. F.; Zhang, W. J. Green synthesis of bifunctional fluorescent carbon dots from garlic for cellular imaging and free radical scavenging. *ACS Appl. Mater. Interfaces* **2015**, *7*, 17054–17060.

[34] Yin, J. J.; Lao, F.; Fu, P. P.; Wamer, W. G.; Zhao, Y. L.; Wang, P. C.; Qiu, Y.; Sun, B. Y.; Xing, G. M.; Dong, J. Q. et al. The scavenging of reactive oxygen species and the potential for cell protection by functionalized fullerene materials. *Biomaterials* **2009**, *30*, 611–621.

[35] Shahzad, A.; Rasool, K.; Miran, W.; Nawaz, M.; Jang, J.; Mahmoud, K. A.; Lee, D. S. Two-dimensional $Ti_3C_2T_x$ MXene nanosheets for efficient copper removal from water. *ACS Sustainable Chem. Eng.* **2017**, *5*, 11481–11488.

[36] Guo, J. X.; Peng, Q. M.; Fu, H.; Zou, G. D.; Zhang, Q. R. Heavy-metal adsorption behavior of two-dimensional alkalization-intercalated MXene by first-principles calculations. *J. Phys. Chem. C* **2015**, *119*, 20923–20930.

[37] Hagfeldt, A.; Bergstrom, R.; Siegbahn, H. O. G.; Lunell, S. Structure and stability of small titanium/oxygen clusters studied by *ab initio* quantum chemical calculations. *J. Phys. Chem.* **1993**, *97*, 12725–12730.

[38] Zhao, X. G.; Huang, J. G.; Wang, B.; Bi, Q.; Dong, L. L.; Liu, X. J. Preparation of titanium peroxide and its selective adsorption property on cationic dyes. *Appl. Surf. Sci.* **2014**, *292*, 576–582.
[39] Zhang, X. F.; Liu, Y.; Dong, S. L.; Ye, Z. Y.; Wei, Y. D. Low-temperature synthesized nanocomposites with amorphous feOOH on $Ti_3C_2T_x$ for supercapacitors. *J. Alloys Compd.* **2018**, *744*, 507–515.
[40] Zhang, G. S.; Fan, F.; Li, X. P.; Qi, J. Y.; Chen, Y. H. Superior adsorption of thallium(I) on titanium peroxide: Performance and mechanism. *Chem. Eng. J.* **2018**, *331*, 471–479.
[41] Ijichi, T.; Itoh, T.; Sakai, R.; Nakaji, K.; Miyauchi, T.; Takahashi, R.; Kadosaka, S.; Hirata, M.; Yoneda, S.; Kajita, Y. et al. Multiple brain gas embolism after ingestion of concentrated hydrogen peroxide. *Neurology* **1997**, *48*, 277–279.
[42] Long, L.; Liu, H. H.; Liu, X. J.; Chen, L. L.; Wang, S. Y.; Liu, C. Y.; Dong, S. J.; Jia, J. B. Co-embedded N-doped hierarchical carbon arrays with boosting electrocatalytic activity for *in situ* electrochemical detection of H_2O_2. *Sensor. Actuat. B: Chem.* **2020**, *318*, 128242.
[43] Rojas, D.; Hernández-Rodríguez, J. F.; Pelle, F. D.; Del Carlo, M.; Compagnone, D.; Escarpa, A. Oxidative stress on-chip: Prussian blue-based electrode array for *in situ* detection of H_2O_2 from cell populations. *Biosens. Bioelectron.* **2020**, *170*, 112669.
[44] Hekimi, S.; Lapointe, J.; Wen, Y. Taking a "good" look at free radicals in the aging process. *Trends Cell Biol.* **2011**, *21*, 569–576.
[45] Xie, J. N.; Wang, N.; Dong, X. H.; Wang, C. Y.; Du, Z.; Mei, L. Q.; Yong, Y.; Huang, C. S.; Li, Y. L.; Gu, Z. J. et al. Graphdiyne nanoparticles with high free radical scavenging activity for radiation protection. *ACS Appl. Mater. Interfaces* **2019**, *11*, 2579–2590.
[46] Zhang, H.; Wang, L. B.; Chen, Q.; Li, P.; Zhou, A. G.; Cao, X. X.; Hu, Q. K. Preparation, mechanical and anti-friction performance of MXene/polymer composites. *Mater. Des.* **2016**, *92*, 682–689.
[47] Zha, X. H.; Zhou, J.; Zhou, Y. H.; Huang, Q.; He, J.; Francisco, J. S.; Luo, K.; Du, S. Y. Promising electron mobility and high thermal conductivity in Sc_2CT_2(T = F, OH) MXenes. *Nanoscale* **2016**, *8*, 6110–6117.
[48] Chen, J. F.; Hu, Q. K.; Zhou, A. G.; Sun, D. D. Theoretical studies of lithium storage properties of novel two-dimensional carbides. *Acta Phys.-Chim. Sin.* **2015**, *31*, 2278–2284.
[49] Martínez, A.; Francisco-Marquez, M.; Galano, A. Effect of different functional groups on the free radical scavenging capability of single-walled carbon nanotubes. *J. Phys. Chem. C* **2010**, *114*, 14734–14739.
[50] Hou, J. J.; Wang, H.; Ge, Z. L.; Zuo, T. T.; Chen, Q.; Liu, X. G.; Mou, S.; Fan, C. H.; Xie, Y.; Wang, L. H. Treating acute kidney injury with antioxidative black phosphorus nanosheets. *Nano Lett.* **2020**, *20*, 1447–1454.
[51] Morita, K.; Suzuki, T.; Nishimura, Y.; Matsumoto, K.; Numako, C.; Sato, K.; Nakayama, M.; Sasaki, R.; Ogino, C.; Kondo, A. *In vivo* tissue distribution and safety of polyacrylic acid-modified titanium peroxide nanoparticles as novel radiosensitizers. *J. Biosci. Bioeng.* **2018**, *126*, 119–125.
[52] Seabra, A. B.; Paula, A. J.; de Lima, R.; Alves, O. L.; Durán, N. Nanotoxicity of graphene and graphene oxide. *Chem. Res. Toxicol.* **2014**, *27*, 159–168.
[53] Steiner, A. A.; Branco, L. G. Carbon monoxide is the heme oxygenase product with a pyretic action: Evidence for a cGMP signaling pathway. *Am. J. Physiol. Regul., Integr. Comp. Physiol.* **2001**, *280*, R448–R457.
[54] Rejman, J.; Oberle, V.; Zuhorn, I. S.; Hoekstra, D. Size-dependent internalization of particles via the pathways of clathrin-and caveolae-mediated endocytosis. *Biochem. J.* **2004**, *377*, 159–169.